Post deposition annealing of praseodymia films on Si(111) at low temperatures

S. Gevers[1], T. Weisemoeller[1], D. Bruns[1], A. Giussani[2], T. Schroeder[2], and J. Wollschläger[1a]

[1] *Fachbereich Physik, Universitt Osnabrück and Center of Interface Science, Barbarastr. 7, D-49069 Osnabrück, Germany*

[2] *IHP, Im Technologiepark 25, D-15236 Frankfurt (Oder), Germany*

(Dated: March 22, 2011)

Abstract

Thin heteroepitaxial praseodymia films with fluorite structure on Si(111) were annealed under ultra high vacuum conditions at temperatures in the region of 100 °C up to 300 °C. Afterwards investigations by X-ray diffraction, grazing incidence X-ray diffraction and X-ray reflectometry were performed to obtain information about structural changes of the film during the annealing process. For this reason, praseodymia Bragg peaks were carefully analyzed within the kinematic diffraction theory. This analysis demonstrates the coexistence of different praseodymia phases depending on the conditions of preparation. Here, annealing of the samples up to 150 °C leads to a homogeneous film with $PrO_{1.833}$ phase and with negligible strain since both the lateral and vertical lattice parameters nearly match the corresponding bulk praseodymia phase. Further annealing leads to oxygen loss accompanied by significantly increased lattice parameters. Since the lateral lattice parameter is pinned at the interface, the vertical lattice constant has to increase considerably due to the tetragonal distortion of the film. This causes the decomposition of the film into two oxide species with significantly different oxygen contents. Annealing at 300 °C reduces the film almost completely to $PrO_{1.5}$ which has the minimum content of oxygen.

[a] Electronic mail: joachim.wollschlaeger@uos.de

I. INTRODUCTION

Due to their dielectric properties and their high oxygen mobility, Rare earth oxides (REOs) are in the focus of ongoing research concerning many important fields of technology. In this manner, applications in microelectronics [1], sensor technology [2] and catalytic reactions [3] are intensively discussed.

In all of these applications, praseodymia presents itself as an ideal model system for fundamental studies since crystalline praseodymia films with different structural phases can be grown on Si substrates [4, 6, 7] representing the dominating semiconductor material platform. In this regard, integrated germanium-on-insulator (GeOI) systems are discussed aiming to boost the sub-45 nm complementary metal oxide semiconductor (CMOS) technologies and further to achieve the cost-effective monolithic integration of III-V optoelectronic materials (GaAs) on the Si wafer platform. This is because the Ge-GaAs system shows only minimal lattice mismatch ($\sim 0.08\%$) and almost no difference of the thermal expansion coefficent between Ge and GaAs in contrast to the Si-GaAs system (lattice mismatch $\sim 4.1\%$ and difference of expansion coefficient $\sim 110\%$, respectively).

Here, praseodymia films serve as high-functional buffer material to enable the growth of high quality Ge films on the Si platform [5, 18]. It is, however, crucial to grow oxide films with homogeneous structure and low defect-density to offer a perfect buffer for the Ge film since defects reduce drastically the electronic advantages of Ge (compared to Si). Therefore, it is necessary to control the lattice misfit between Ge film and praseodymia buffer, which depends strongly on the preparation conditions of the oxide film (see below). This assures the excellent properties of the praseodymia buffer layer, which directly influences the functionality of the GeOI multilayer structures. Therefore, detailed analysis of the oxide film structure is necessary to control these important properties and to further improve the quality of the buffer layers. For this purpose, X-ray methods like XRD and XRR turn out to be a powerful tool to determine the complex structure of these multilayer systems.

Furthermore, praseodymia offers the highest oxygen mobility compared to the other REOs [8]. Thus praseodymia is advantageous for catalytical applications. For instance, it is known to be catalytically active in several reactions like CO and NO oxidation, dehydration, dehydrogenation and alkylation of organic compounds [9–11]. According to the occuring Mars-van-Krevelen mechanism, where lattice oxygen is involved in the redox-reactions at

the surface, the high oxygen mobility and storage capacity of the praseodymia films plays an important role [12, 13]. Furthermore, this high oxygen mobility causes wide range of different oxide phases in the praseodymia (PrO_x) phase diagram. Here, the well known oxide phases PrO_2 and cubic Pr_2O_3 (cub-Pr_2O_3) represent the highest and the lowest oxidation states. Additional ordered crystalline oxide phases can be found in the region of $PrO_{1.833}$ to $PrO_{1.714}$. Although many oxide phases can be found here, cub-Pr_6O_{11} (x=1.833) is the most prominent oxide phase in this region. Between this intermediate phase region and both extreme oxidation states Pr_2O_3 and PrO_2 miscibility gaps can be found [21].

However, all catalytical applications require a specific reaction temperature and therefore the development of several post deposition annealing (PDA) procedures. Since the praseodymium-oxygen system as well as the availability of lattice oxygen is strongly dependent on sample temperature and partial oxygen pressure, it is crucial to study the behavior of praseodymia films under PDA conditions. This includes the changes of oxygen content within the oxygen film which is accompanied by changes of the crystalline structure.

Recent work suggests that PDA under ultra high vacuum (UHV) conditions leads to a full phase transition of praseodymia films from fluorite to bixbyite (PrO_2 to cub-Pr_2O_3) structure already at 300 °C [14]. A significantly increased unit cell has to be formed during the process of oxygen loss since a decreased oxygen content leads to the formation of Pr^{3+} ions which have a larger ionic radius than Pr^{4+} ions. This results in laterally strained films with mosaics at the surface of the praseodymia films [14].

In the work presented here, we investigate the PDA process of praseodymia films with fluorite structure at a lower annealing temperatures (100 °C to 300 °C). The goal is to get a deeper understanding of the processes which lead to the phase transition of the unit cell and to get a more precise view of the process of oxygen loss during PDA in UHV. Furthermore, additional lateral information of the crystalline structure are extracted to comprehend the occurring strain mechanisms. Finally, a sophisticated model of the PDA process is established, using X-ray diffraction analysis within the kinematic diffraction theory.

II. EXPERIMENTAL

Ultra thin films of hexagonal Pr_2O_3 (hex-Pr_2O_3) structure with 10 nm film thickness were deposited on clean boron-doped Si(111) substrates ($\rho = 5$-$15\,\Omega$cm off-normal orienta-

tion = $(0.35 \pm 0.15)\,^\circ$) as reported previously by Schroeder et al. [6]. These samples were annealed in 1 atm oxygen at 700 °C for 30 minutes to obtain heteroepitaxial PrO_2 films with fluorite structure ($Fm\bar{3}m$ in Hermann-Mauguin notation) [7].

To study structural changes during thermal treatment, additional annealing of the samples was applied afterwards by resistive heating in UHV (base pressure $1 \cdot 10^{-10}$ mbar) at a temperature range from T = 100 °C to 300 °C. To determine the structure of these oxide films, X-ray measurements were performed at beamlines BW2 and W1 at DESY (Hamburg, Germany). Both beamlines are equipped with six circle diffractometers. We used 10.0 keV photons to conduct X-ray reflectometry (XRR), X-ray diffraction (XRD) and grazing incidence X-ray diffraction (GIXRD) measurements.

The vertical structure of the films was acquired by XRR and XRD measurements, which were performed in $\theta - 2\theta$ geometry with a variable incidence angle. By using a linear X-ray photon detector, additional lateral information (especially close to Bragg peaks) was obtained during data recording. GIXRD measurements were carried out with a fixed incidence angle of 0.5° well above the critical angles for praseodymia (0.28 °) and Si (0.18 °). From these experiments, the lateral structure of the films was determined.

III. RESULTS

A. X-Ray Diffraction and Gracing Incidence X-Ray Diffraction

Specular $\theta - 2\theta$ scans of the samples with different annealing temperatures are presented in Fig. 1. Here, L denotes the absolute value of the scattering vector $Q_\perp$ normal to the surface in reciprocal relative lattice units scaled to the silicon layer distance (d_{Si}) via $L = d_{Si}Q_\perp/2\pi$. Therefore, the Bragg peaks denoted by $Si(LLL)_B$ in bulk notation are equivalent to $Si(00L)_S$ Bragg peaks in surface coordinates due to the (111) orientation of the Si substrate.

Strong and sharp Si-Bragg peaks can be observed in all measurements at $L = 1$ and $L = 3$ since the penetration depth of the X-ray beam for the used incidence angles is always higher than 2300 nm for Si, but only 70 nm for praseodymia. Therefore, sharp Si signals are visible in both XRD and GIXRD measurements, which can be used for precise calibration of the oxide Bragg peak positions [7]. The Si Bragg peaks at $L = 2$, however, are kinematically forbidden and only small intensity can be detected due to deviations from the spherical

electron distribution of the Si atoms. Broad Bragg peaks of the thin oxide films are located near the Si-peak positions. These peaks exhibit additional intensity oscillations (fringes) due to high crystalline quality of the praseodymia films, their sharp interfaces and their homogeneous thickness.

The region at $L \approx 1$ is not well suited for detailed oxide film analysis since strong interference effects occur between Si substrate and oxide film. Those effects are enhanced and complicated by an amorphous silicate interface which acts as a spacer between the two crystalline structures [17]. Hence, in the following, the region at $L \approx 2$ is used for crystal truncation rod (CTR) analysis since the praseodymia peak intensity is still adequate for detailed analysis while the Si peak intensity is small. Thus, only little interference effects are observed at this position in reciprocal space since the Si Bragg peak intensity, on the one hand, is sufficiently strong to calibrate the position of the broader oxide Bragg peak but, on the other hand, sufficiently weak to suppress film-substrate interference.

For the untreated sample (RT), a first glance at the region of $L \approx 2$ shows two clearly distinguishable praseodymia Bragg peaks positioned on the left and the right side of the sharp Si Bragg peak. This can be explained by two laterally coexisting oxide species with different vertical lattice constants [7, 14]. Apparently, after annealing of the sample at 100 °C only one Bragg peak remains on the left side of the Si Bragg peak. This is also observed at higher annealing temperatures up to 300 °C. The detailed analysis presented below, however, will show that still two oxide species have to be assumed although only *one* obvious Bragg peak seems to exist. The position of the obvious Bragg peaks shifts to lower L-values with higher annealing steps (150 °C - 300 °C). Furthermore, the (01L) crystal truncation rods (CTR, cf. Fig. 2) exhibit main oxide Bragg peaks at $L \approx 0.33$ and $L \approx 1.33$ for all annealing steps. These positions are expected for cubic structure with *exclusive* B-type orientation [17] since no Bragg peaks can be found at $L \approx 0.67$ (Bragg condition for A-type stacked cubic structure).

Regarding the samples annealed at temperatures lower than 150 °C, additional weak and broad Bragg peaks appear close to half integer positions in (00L) direction beside the main oxide peaks (cf. Fig. 1). These peaks slightly shift with higher annealing temperature from $L = 1.490 \pm 0.005$ and $L = 2.488 \pm 0.005$, respectively, for the untreated sample to $L = 1.484 \pm 0.005$ and $L = 2.474 \pm 0.005$, respectively, after annealing at 150 °C in agreement with the shifts of the oxide Bragg peaks. Furthermore, the intensity of these peaks gradually

increases after annealing at 100 °C and 150 °C until they vanish after annealing at 200 °C. Since the Bragg condition for the hexagonal Pr_2O_3 oxide structure is fullfilled at considerable higher L-values (L_{hex}=1.563), these peaks are caused by vertically ordered superstructures (probably due to periodically arranged oxygen vacancies accompanied by partial rearrangement of the Pr sublattice and inducing a doubling of the praseodymia vertical lattice spacing [14, 17]). This finding is supported by the analysis of the (01L) CTRs where small Bragg peaks can be found at $L \approx 0.83$ fulfilling the corresponding Bragg condition for the twofold superstructure (cf. Fig. 2). These peaks also show the same behavior with higher annealing temperature regarding peak position and intensity as the peaks found in (00L) direction.

After annealing at 200 °C another broad peak of small intensity appears in (00L) direction, but it is only visible at $L = 0.77$ (cf. Fig. 1). This peak is also visible after annealing at 300 °C but it is broadened compared to the former annealing step. Regarding the (01L) CTR, additional Bragg peaks are also present at the corresponding positions. They are slightly better visible at higher L-values. Their intensities, however, strongly decrease with higher L-values. This small intensity in conjunction with the absence of fringes makes a detailed analysis of these peaks difficult. However, the peak positions on (00L) and (01L)-CTR demonstrate that this species has cubic crystalline structure. The FWHM of the Bragg peaks points to a thickness of about five mono layers which seems to decrease after annealing at 300 °C.

Fig. 3(a) shows exemplary in-plane scans for the untreated sample and the samples annealed at 100 °C and 300 °C, respectively. The scans were performed in $(0K0)_S$ direction parallel to the surfaces of the samples with $L = 0.05$. The region at $K \approx 3$ was studied since both the Si substrate and different praseodymia phases exhibit Bragg peaks here. Thus, the lateral lattice parameter of the oxide species in question can be determined for all annealing temperatures.

Regarding the measurement of the untreated sample, a broad praseodymia Bragg peak can be found at lower K values than the sharp Si Bragg peak which is located at $K = 3$. This peak position can also be observed after any annealing step. However, annealing at 300 °C leads to a slight shift of the oxide peak to lower K values.

In principle, determining the lateral lattice parameters $a_{||}$ is difficult since it is possible that the Bragg peak consists of two or more subpeaks with slightly different peak positions as expected from the coexistence of different praseodymia phases with different *vertical*

lattice constants (see above). This assumption would explain the significant broadening of the in-plane oxide peaks with higher K-values which will be discussed in detail later on. A discrimination of these subpeaks is nearly impossible since no distinct separation of the peaks can be observed. Therefore, we assume a single Bragg peak for any annealing step to calculate mean lateral lattice parameters which are shown in Fig. 3(b). As discussed later on, the accuracy of these values are still sufficient to estimate the stoichiometry of the oxide species.

Weisemoeller et al. reported that the lateral lattice parameter of the oxide film was exclusively pinned to the bulk value of hex-Pr_2O_3 which is about 0.22 % smaller than bulk Pr_6O_{11} ref. [17]. Here, however, all investigated samples exhibit lattice constants which are slightly bigger than the expected bulk value of Pr_6O_{11}. Therefore, it is reasonable that the lateral pinning of the oxide film is not as well defined as reported previously. The lattice parameter of $a_{||} = 387 \pm 1$ pm is derived for the untreated sample. Within the error bars, this value is unchanged until annealing at 300 °C. Here, a slight increase of the lattice parameter to $a_{||} = 389 \pm 1$ pm is observed which points to a disintegration of the lateral pinning with higher annealing temperatures. Regarding the bulk values of cub-Pr_2O_3, however, considerable pinning effects still have to be taken into account.

As explained above, a detailed analysis of the $PrO_x(222)_B$ peak intensity was performed to determine the *vertical* film structure after annealing in UHV. This was done by calculating the intensity distributions at $L \approx 2$ within the kinematic diffraction theory which gives information about the vertical lattice parameters $a_\perp$ (position of the Bragg peaks) as well as the crystalline layer thicknesses D (periodicity of fringes). The model which was used to perform the intensity calculations is based on our former work [14] where it was concluded, fitting the Bragg peak intensities with Gaussian functions, that two oxide species (called columns) coexist *laterally* if the samples were annealed in UHV at higher temperatures (300 °C - 600 °C). Nevertheless, if this simple model is applied to the more sophisticated analysis based on the kinematic diffraction theory (including the appearing fringes) some modifications are necessary to obtain good agreement with the data presented here. A detailed description of this structure model and the used fitting parameters is given in the Appendix.

To describe these modifications the evolution of the model for the untreated sample is presented in Fig. 4. First, the former established model of two coexisting *homogeneous*

columns is applied to analyze the diffracted intensity. The vertical lattice constants obtained by this analysis show that the oxide species can be attributed to $PrO_{1.833}$ (Bragg peak for $L < 2$) and PrO_2 (Bragg peak for $L > 2$), respectively (see below). The $PrO_{1.833}$ species has less oxygen content compared to the PrO_2 oxide species and therefore causes additional intensity at *lower* L values. Fig. 4(a) shows that the Bragg peak at lower L values is described well by the model calculation whereas the other peak is not reproduced that well. Furthermore, the regions at lower and higher L values (fringes) show only poor agreement between the calculated and the measured data. Next step is to decrease the layer thickness of the PrO_2 oxide species corresponding to the Bragg peak at higher L values to increase its FWHM. This leads to a better agreement between the Bragg peak intensity and the calculation (cf. Fig. 4(b)). The position of the fringes at higher L values are also better described, but at lower L values the calculated data exhibits considerable less intensity than the measured intensity. This effect is compensated by adding a small oxide fraction of $PrO_{1.833}$ below the PrO_2 species which corresponds to the Bragg peak at higher L values (cf. Fig. 4 (c)). Finally, an excellent agreement between calculation and measurement is achieved.

We analyzed all experiments assuming this model that one column is homogeneously built by one oxide species while the second column contains a minority and a majority species on top of the interface layer. All samples showed this distribution of oxide species except the one annealed at 100 °C where the additional minority oxide species did not lead to improvements. Here, both columns have the same layer thickness and are homogeneous (cf. Fig. 5). To match the experimental data of the other samples it has to be taken into account, that the small oxide fraction can also exhibit higher oxygen content compared to the majority oxide species which results in additional intensity at *higher* L values compared to the main oxide peak. This can be observed for example after annealing at 200 °C. Furthermore, the position of the minority oxygen species concerning the annealed samples is either on top of the majority oxide part if the oxygen content is *lower* or below the majority part if the oxygen content is *higher* compared to the majority oxide species. In all cases, the simulation of the intensity distributions with the modified structure model leads to excellent agreement with the measured data (cf. Fig. 5) and every simulation results in two laterally separated oxide species although only one apparent oxide Bragg peak can be seen at $L \approx 2$. This is in agreement with previous works [7, 14].

Fig. 6 presents the resulting vertical lattice constants $a_\perp$ of the films which were derived from our model. The untreated sample (RT) exhibits two significant different values for $a_\perp$, which can be assigned to each oxide species. While the lattice constant of the majority part (majority and minority parts are indicated with dots and squares, respectively) of the inhomogeneous column $a_\perp^{(1)}$ ($a_\perp^{(1)}$ is indicated by full symbols) is smaller compared to the bulk value of PrO_2, the lattice parameters of the minority part $a_\perp^{(1')}$ and the homogeneous column $a_\perp^{(2)}$ ($a_\perp^{(2)}$ is indicated by open symbols) exhibit almost identical values of between the bulk values of PrO_2 and Pr_6O_{11}. Annealing the samples to higher temperatures leads to an increase of these lattice constants. First, after annealing at 100 °C where no minority species can be observed, $a_\perp^{(1)}$ and $a_\perp^{(2)}$ converge close to the bulk value of Pr_6O_{11}. Further annealing at 150 °C results in a slight increase of the lattice parameters of the majority parts of the film. However, a minority part can be observed again with a significant larger vertical lattice constant $a_\perp^{(2')}$ (open squares). Stronger changes are detected after annealing at 200 °C. Here, $a_\perp^{(1)}$ is still closer to the lattice constant of Pr_6O_{11}, but $a_\perp^{(2)}$ increases significantly beyond the bulk value of cub-Pr_2O_3. The lattice constant of the minority part of the inhomogeneous column $a_\perp^{(2')}$ is also closer to the lattice constant of Pr_6O_{11}. After annealing at 300 °C both values of the majority film parts as well as the minority part are larger than the bulk value of cub-Pr_2O_3. Here, $a_\perp^{(2)}$ is considerably stronger increased compared to the bulk value (+1.8 %) than $a_\perp^{(1)}$ and $a_\perp^{(2')}$. Again the minority part shows a lattice constant $a_\perp^{(2')}$ close to the smaller value of $a_\perp^{(1)}$.

Since the loss of oxygen atoms is accompanied by the forming of Pr^{3+} ions, which exhibit a bigger ion radius than Pr^{4+} ions, the unit cell of the praseodymia film will increase with decreasing oxygen content. Therefore, it is possible to infer the oxygen content of the oxide species from the value of the lattice parameters. However, to attribute the oxide species to particular oxide phases, it is necessary to take into account both the *vertical* and *lateral* lattice constants since the bulk structure is distorted in films. Because of the lateral pinning, the *expected* bulk vertical lattice parameters are corrected *assuming* a tetragonally distorted unit cell and a Poisson ratio of $\nu = 1/3$ [7, 18]. In doing so, the tetragonal distortion is described by

$$\frac{\Delta a_\perp}{a_\perp} = -\frac{\Delta a_{||}}{a_{||}}.$$

Since a distribution of the lateral lattice parameters cannot be excluded, it is impossible to determine exactly the lateral pinning of the particular oxide species and therefore, the

expected vertical lattice parameters. Thus, the uncertainty of the expected $a_\perp$ values (based on the uncertainty of the lateral lattice parameters determined from in plane measurements) are given by colored regions in Fig. 6 for PrO_2, Pr_6O_{11} and cub-Pr_2O_3.

Regarding the majority crystalline oxide parts (indicated by open and full dots in Fig. 6), the untreated sample exhibits two different stoichiometries. One oxide species has a vertical lattice constant within the upper region expected for PrO_2, while the vertical lattice parameter of the other species is located in the Pr_6O_{11} region. After annealing at 100 °C and 150 °C, both species exhibit similar values of $a_\perp$ which are in the Pr_6O_{11} area. Annealing at 200 °C leads to an increase of both lattice constants whereas one lattice constant is stronger increased so that again both lattice constants are separated significantly. One of the lattice constants is very close to the expected value of cub-Pr_2O_3 and the other value is closer to Pr_6O_{11}. Further increase of the vertical lattice parameters can be observed after annealing at 300 °C. Here, $a_\perp$ of one of the oxide species is located within the upper cub-Pr_2O_3 region, whereas the other vertical lattice parameter is slightly smaller than expected for cub-Pr_2O_3.

The vertical lattice constants of the minority crystalline parts are indicated with squares in Fig. 6. For the untreated sample and the sample annealed at 150 °C, the lattice constants of the minority species are larger than the lattice constants of the majority oxide species. This is attributed to an enhanced oxygen loss within these parts compared to the initial PrO_2. The samples annealed at 200 °C and 300 °C, however, exhibit small crystalline parts with more oxygen content compared to the corresponding majority parts since their lattice constants are significantly smaller. Except the sample annealed at 150 °C all additional fractions show similar values compared to the second oxide species, respectively.

The layer thicknesses D, of the different oxide species are presented in Fig. 7. If the majority and minority oxide parts of the inhomogeneous columns are added, both columns exhibit similar overall layer thicknesses for any annealing step. These thicknesses stay nearly constant up to an annealing temperature of 150 °C. Only a slight increase of the overall film thicknesses can be detected due to the increasing vertical lattice parameter induced by the loss of oxygen. A significant decrease of the layer thicknesses, however, occurs after annealing at 200 °C and 300 °C, respectively. Here, about 1 nm of the crystalline oxide film is lost. This can be attributed to the increased silicate layer at the interface and the contamination of the film with hydroxides as it is shown in detail in the XRR results (see below). Furthermore, the difference between overall thicknesses and majority parts shows that the minority oxide

species which were added to the majority fractions, as mentioned before, exhibit thicknesses in the region of several mono layers which is indeed small compared to the main oxide parts.

Additional information about crystalline sizes and mosaic angles can be derived by analyzing the behavior of the in-plane FWHM of the Bragg peaks for different L values. One of these reciprocal space mappings (rsm) is shown exemplarily for the untreated sample in Fig. 8(a). Here, the rsm close to the (00L)-CTR between L=0.8 and L=2.1 is presented (see lower axis for L values). At $L \approx 1$ a sharp, but intense Si peak can be observed (indicated by the open triangle). Additional broad intensity in this region is caused by the oxide Bragg peak which can be found more clearly at $L \approx 2$ at explained above. Beside the Bragg peaks oscillations with less intensity occur which can be assigned to the fringes. First step is to determine the FWHM of in plane scans close to the maximum of each oxide Bragg peak. This is performed by fitting the Bragg peaks with Gaussian functions, as it is shown exemplarily for the oxide Bragg peak at higher L values compared to the Si Bragg peak position marked with triangles (red lines in Fig. 8 (a)). Beside the oxide signal, additional intensity from the Si signal can be observed, especially close to $L \approx 1$ (PL1). However, both signals can be distinguished well since the Si signal is sharp compared to the oxide intensity distribution.

Fig. 8(c) presents the obtained FWHMs close to $L \approx 1$ and $L \approx 2$ for the untreated sample and all annealed samples, respectively. The untreated sample exhibits two distinguishable FWHM minima close to $L \approx 2$ which can be attributed to the differed oxide species. At $L \approx 1$, the minima positions are converged, but they still can be separated. After determining the positions of the FWHM minima, a straight line can be calculated for each oxide species (dashed and dotted lines). From this, the corresponding, mosaic spreads can be derived by the inclination of the lines and the reciprocal value of the crystallite sizes $D_{||}$ are determined from the intersection of the lines with the ordinate, respectively.

These values has been determined for each majority oxide species since the behavior of the FWHM can be considered separately. However, after any annealing step only a single minimum of the FWHM can be detected at $L \approx 1$ and $L \approx 2$, respectively. This effect is caused by the very small separation of the oxide Bragg peaks in L-direction mentioned above. Here, only one value of crystalline size and the mosaic angle has been calculated for both majority oxide species. The minority crystalline parts of the samples cannot be analyzed with this method since their intensity is too low and dominated by the fringe

intensity.

The resulting values of the average lateral crystallite size and the mosaic spread are presented in Fig. 9(a) and (b), respectively. For the untreated sample, the crystallite sizes $D_{||}$ are (48 ± 3) nm and (64 ± 10) nm. They can be attributed to the Pr_6O_{11} and PrO_2 oxide species, respectively. Annealing to 100 °C and 150 °C leads to a stepwise increase of $D_{||}$ to (100 ± 9) nm which is is an average value for both oxide species, as described before. After annealing at 200 °C the average crystallite size decreases drastically to 52 nm which stays nearly constant with further annealing at 300 °C. The two mosaic spreads determined for the untreated sample are very similar so that a mean value of $(0.273 \pm 0.015)^\circ$ is derived. With increasing annealing temperature, the average mosaic spread also increases and finally becomes $(0.345 \pm 0.011)^\circ$ after annealing at 300 °C.

B. X-Ray Reflectometry

Fig. 10(a) shows the XRR measurements of the differently annealed samples and the corresponding calculated intensities following the Parratt algorithm [15]. All measurements exhibit well defined intensity oscillations (fringes) pointing to homogeneous film structures. Whereas the samples annealed at temperatures up to 150 °C show very similar intensity distributions, a significant damping of the fringes can be observed for the sample annealed at 200 °C, which indicates an increased film roughening. After annealing at 300 °C, the fringes are stronger again due to a recovered film homogeneity.

To calculate the intensity distributions a basic model was used, consisting of the praseodymia film on top of a (Pr-rich) silicate interface layer above the Si substrate [14, 17]. Ono et al. reported another silicate layer with low Pr concentration between the Pr-rich layer and the substrate [16]. This layer, however, was neglected since the electron densities of the Si substrate and the Pr-poor silicate are too similar to obtain reliable data with XRR [7]. Furthermore, based on the fact that the oxide film splits into two laterally separated columns with slightly different structural properties (cf. XRD results), a two-column model was also used in the entire XRR analysis to model the data.

For the untreated sample and the first two annealing steps this basic model leads to excellent agreement with the measured data, but for the samples annealed at 200 °C and 300 °C, this model has to be modified to describe the XRR data, respectively. Here, a third

layer for both columns with significantly lower electron density compared to the oxide was assumed on top of the praseodymia film to describe the effects of the additional crystalline part, which was observed in the XRD measurements. Our XRR calculations suggest that the additional film is at the surface, which can be explained by contamination of the surface near praseodymia mono layers during the storage in normal atmosphere, as discussed in detail later on. Fig. 10(a) shows that calculations of the reflected intensities with the proposed models lead to excellent agreement with the experimental data.

Comparison of both columns shows that all parts of the films exhibit similar layer thicknesses after each annealing step (cf. Figure 10(b)). The thickness of the oxide film corresponds completely with the overall praseodymia thickness calculated from the XRD measurements. The mean Pr-rich silicate thickness of the untreated sample ($I_{XRR} = 2.6 \pm 0.5\,\mathrm{nm}$) is in good agreement with previous studies [7, 14]. Furthermore, slight increase of the interface layer with higher annealing temperatures can be obtained ($+(\,1.3 \pm 0.5)\,\mathrm{nm}$) after annealing at 300 °C.

The additional layer on top of the crystalline oxide shows a slightly lower thickness of $1.6 \pm 0.5\,\mathrm{nm}$ after annealing at 300 °C compared to $2.0 \pm 0.5\,\mathrm{nm}$ after annealing at 200 °C. This result agrees well with the decreased thickness of crystalline oxide determined by XRD. Thus, the growth of silicate interface and the additional surface layer with overall thicknesses of $2.5 \pm 1\,\mathrm{nm}$ (200 °C) and $2.7 \pm 1\,\mathrm{nm}$ (300 °C) agrees well with a simultaneous loss of about 1 nm crystalline oxide material (cf. XRD results in Fig. 7), so that both XRR and XRD analysis offer a consistent model of the praseodymia films.

IV. DISCUSSION

The main goal of the here presented work is to assign the different oxide species, which appear during the annealing process, to particular oxygen phases. As we will show in the following, it is possible to determine the oxygen content of the species, but it is impossible to identify a certain unit cell structure based on the known literature bulk structures. At first, it has to be taken into account that all cubic and pseudo-cubic bulk praseodymia unit cells are based on the fluorite structure. While the cation sublattice undergoes only little positional changes, the different oxide phases are formed by removing and displacing the oxygen atoms since they are extremely mobile in the Pr-O system [27]. Thus, the equilibrium oxide phase

is determined by oxygen pressure, temperature [19, 20]. It is also important to note that the kinetics of the oxidation or reduction processes determine the time which is necessary to reach the equilibrium state. The well known bulk stoichiometries indicate equilibrium states of the Pr-O system on which the material converge at the corresponding ambient conditions. It is reasonable that similar equilibrium states also occur in thin oxygen films where they are referred to specific oxygen contents although influences from interfaces and surfaces may have some impact on the equilibrium.

As reported in literature, huge unit cells were often proposed to describe the crystalline phases of different stoichiometries between PrO_2 and Pr_2O_3 [27, 28]. These point to a long range ordering of the praseodymium and oxygen ions within the bulk material, depending on the ambient conditions. Therefore, it seems probable that little changes concerning strain effects also have a strong impact on the crystalline ordering of the oxygen atoms. As shown here and in former works, the lattices of thin crystalline films on Si(111) are laterally pinned and only slight relaxations can be observed during the annealing process. Thus, ultra thin praseodymia films are significant tetragonally strained. This probably changes the ordering mechanisms of the oxygen sublattice leading to new structures which cannot be obtained in bulk praseodymia, e.g. the twofold vertical periodicity in praseodymia *films* reported here (as well as before [7, 14]) which has not been observed for the *bulk*.

In this work, the Bragg peaks at half integer positions in (00L) direction which appear until annealing at 150°C can clearly be attributed to a cubic structure (probably with vertically ordered oxygen vacancies). Our results show that the lattice parameters of these structures are mostly close to tetragonally strained Pr_6O_{11} bulk structures. Since the corresponding bulk structure exhibits no ordering of the oxygen vacancies which would explain the Bragg peaks mentioned above we will call this structure $PrO_{1.833}$ in the following to distinguish it from bulk Pr_6O_{11}. As it will be discussed later on, this stoichiometry exhibits only little lateral strain, but the influence on the ordering of the oxygen sublattice is distinctive. Therefore, the film of this stoichiometry is an excellent example for the assumed effect of strain on the unit cell structures. Since, that the determined film structure cannot be assigned one to one to known bulk structures, which depend on the oxygen stoichiometry, we will identify the obtained stoichiometries in the following as PrO_x, where x denotes the oxygen content. Although many crystal oxide phases can be found in the region of $PrO_{1.833}$, as mentioned above, it is impossible to distinguish between them because of the similar

lattice parameters. Therefore, we will refer to the oxide species only with $PrO_{2.0}$, $PrO_{1.833}$ and $PrO_{1.5}$ because we can clearly distinguish them (cf Fig. 6). Here, $PrO_{1.833}$ takes on a special position since it marks the border between the intermediate phase region and the miscibility gap to PrO_2.

Fig. 11 presents the schematical model of the annealing process up to 300 °C. The starting sample at RT exhibits the well known structure with two laterally coexisting oxide species. Compared to previous investigations [7, 14, 17], however, two important differences are observed. On the one hand, the oxide species previously denoted as $PrO_{2-\Delta}$ clearly exhibits lattice parameters corresponding to the $PrO_{1.833}$ stoichiometry. Because hex-Pr_2O_3 was oxidized in 1 bar oxygen to achieve cubic structure, it is reasonable that the film is completely oxidized to $PrO_{1.833}$ first before it is further oxidized to $PrO_{2.0}$ due to the miscibility gap between these phases and the lateral pinning to bulk Pr_6O_{11}. Therefore, this structure can undoubtedly be identified as $PrO_{1.833}$ phase. On the other hand, a small fraction of the PrO_2 column is not completely oxidized and also shows $PrO_{1.833}$ structure which can only be identified using a detailed analysis based on calculations within the kinematic diffraction theory. The oxidization of this column is probably incomplete due to the induced strain at the PrO_2 interface, where the film is pinned laterally to the lattice constant of bulk Pr_6O_{11}. Thus, it becomes difficult to incorporate additional oxygen close to the interface, since this decreases the lattice parameter and increases strain.

Annealing at 100 °C leads to a praseodymia film where the praseodymia of both columns is completely reduced to $PrO_{1.833}$. The direct transformation of the PrO_2 oxide species to $PrO_{1.833}$ is explained by the miscibility gap between these phases without any phase with intermediate stoichiometry [21]. The slightly different vertical layer distances are attributed to the distribution of the lateral lattice parameter and small variations of the oxygen content. Since only two different vertical layer distances are determined, it is reasonable that the in plane Bragg peak close to $K \approx 3$ also consists of two subpeaks, which are responsible for the peak broadening at higher K-values. Fitting of the measured peaks with two subpeaks is possible, but the results are ambiguous since the peaks are not very well separated. The analysis of reflections at larger K-values may solve this problem, but significant higher photon energies, than used in the current experimental setup, are necessary to measure these spots since the reflex positions are far out in the reciprocal space (e.g. $K = 6$).

Further annealing at 150°C results in a slight increase of the lattice parameters of the

main oxide fractions. They also show the smallest difference between each other compared to the other annealing steps. This points to a relaxation of the former strained oxide species in this temperature region. Here, both the lateral and the vertical lattice parameter are close to bulk $PrO_{1.833}$. Furthermore, the average crystallite size is at its maximum value. Thus, both majority oxide species may converge into one phase, which is adapted almost perfectly to the Si substrates, so that the film is very homogeneous. The stoichiometry of this phase, however, is not stable under UHV conditions. Thus, at this annealing temperature, a small fraction of one part (cf. right column in Fig. 11) exhibits a significant smaller oxygen content compared to the main oxide species. This is because a praseodymia species with less oxygen content nucleates at this temperature and consumes parts of the $PrO_{1.833}$ phase. The oxide species with less oxygen content is located on top of the film (cf. Fig. 11) because we assume that the surface near region of the film is reduced first since less strain is expected here due to the lack of next neighbors. Although the vertical lattice constant of the minority phase is clearly larger than expected for $PrO_{1.833}$ we cannot attribute this species to a certain oxide phase as mention above. Since significant less oxygen content has to be assumed here, we call this species $PrO_{1.833-\Delta}$, where Δ labels the oxygen deficiency.

The sample annealed at 200°C shows considerable different oxygen contents of both majority species, respectively. Whereas one species can be allocated to $PrO_{1.833-\Delta}$, the other species exhibits a considerable larger vertical lattice parameter close to the expected minimum value for strained Pr_2O_3. Former studies showed that the miscibility gap between the intermediate region and $PrO_{1.5}$ is not as well defined as the gap between the intermediate region and $PrO_{2.0}$ [22]. In particular, during reduction additional oxidation states may be formed. Here, it is also difficult to attribute the structure to a distinct oxide phase. Therefore, we will identify this structure with $PrO_{1.5+\Delta}$ because the vertical lattice constant is smaller, but close to the minimum value of strained Pr_2O_3, which points to a slightly larger oxygen content compared to $PrO_{1.5}$. Thus, it is likely that the oxygen loss due to the annealing process is kinetically hindered here. Furthermore, the phase transition to $PrO_{1.5+\Delta}$ is not completely fulfilled since a small fraction still features an oxygen content of $PrO_{1.833-\Delta}$. Assuming a needle-like growth front of the $PrO_{1.5+\Delta}$ phase into the preexisting $PrO_{1.833-\Delta}$ species, it is reasonable that the minority fraction $PrO_{1.833-\Delta}$ is located close to the interface of the film.

The significant difference between the vertical lattice parameters of both oxide species

implies that the strain within the film is considerable increased. A decrease of the mean crystallite size is also observed. This can be interpreted as follows: First, the strain within the film is decreased since vertical and lateral lattice parameter shift towards a value which is close to the almost unstrained bulk value of $PrO_{1.833}$. Further annealing reduces the film partly, and it decomposes into smaller crystallites with different oxygen contents. This increases the equilibrium lattice parameters within the reduced regions in both lateral and vertical direction. Therefore, lateral pressure is applied to the regions with higher oxygen content. This leads to an increasing energy barrier to remove oxygen atoms from the strained regions. For this reason, one region of the film still shows significant higher oxygen content compared to the other region which is further reduced. This is supported by the results of Rudenko et al. who also reported for bulk material that praseodymia tends to coexist in different oxidation states [23]

With annealing to 300°C a similar film structure compared to the sample annealed at 200°C can be observed. However, the thermal energy is sufficiently large to remove more oxygen from the film. Because of this, one of the majority species shows a vertical lattice parameter within the region of strained $PrO_{1.5}$. Although it is not completely reduced and a small part of the column still shows structure parameters of $PrO_{1.5+\Delta}$. This effect is comparable to the splitting of the column after annealing at 200°C. The other phase exhibits a vertical lattice parameter just below the region expected for $PrO_{1.5}$, but significantly smaller compared to the first species. Thus, the second phase has a larger oxygen content and has to be identified with a $PrO_{1.5+\Delta}$ phase.

Furthermore, it seems that the temperatures which are necessary to reduce the film towards $PrO_{1.5}$ are much lower than the values reported previously by Hyde et al. [22] for bulk praseodymia. In this work, it was also shown that the temperatures necessary to obtain $PrO_{1.5}$ decrease with decreasing oxygen pressure. Therefore, the low values obtained in the present work can be explained since we used a base pressure of $1 \cdot 10^{-10}$ mbar compared to several 10 mbars used by Hyde et al. [22].

The exact stoichiometry of bulk $PrO_{1.5}$ is energetically favorable only for the hexagonal phase while the incorporation of small amounts of oxygen directly leads to a phase transformation to cub-Pr_2O_3 [23, 24]. Therefore, the cubic $PrO_{1.5}$ phase obtained here has probably also to be identified as a $PrO_{1.5+\delta}$ phase. Whereas the δ is significantly smaller than the Δ of the $PrO_{1.5+\Delta}$ phase reported above. Thus, we conclude that the sample annealed at

300°C is not completely reduced to $PrO_{1.5}$ as previously reported [14]. This effect can be attributed to the lateral strain within the film, which increases with further oxygen loss, so that additional strain relaxation mechanisms have to be considered for full reduction. This can be achieved tilting the crystal planes with respect to the surface. Increased mosaic angles for example are reported for samples annealed at 600°C under UHV conditions [14]. Here, almost identical vertical lattice constants were found for both oxide species which are less separated than the ones found for the sample annealed at 300°C.

The crystallite sizes obtained in previous reports [7, 17] exhibit a lower limit of about 11 nm whereas in this work we determined values which are at least four times larger. This can be explained by the different methods used to calculate the grain sizes. In the former work, the FWHM of the *in-plane* oxide Bragg peaks at $K \approx 3$ were determined and the grain size was directly derived applying the Scherrer formula. However, the possible distribution of the lateral lattice constants due to different phases, which was also previously reported, would cause an additional broadening of the Bragg peaks with increasing K-value. Therefore, the calculation of the crystallite sizes would systematically result in too small values. This can be avoided with the presented method, where the FWHM of *out-of-plane* oxide Bragg peaks of the (00L)-CTR has been extrapolated for $L \to 0$.

The mosaic angle spread measured in the present work increases with increasing annealing temperature which points to a starting relaxation process. The mosaics exhibit no preferred orientation which is comparable to the mosaics previously observed for annealing at higher annealing temperatures [14]. However, the spread of the angles is significant smaller than reported for 600°C, so that the lateral strain cannot be completely reduced here. Furthermore, in the former work two mosaic angles were obtained by spot profile analysis low energy electron diffraction (SPA-LEED) measurements for samples annealed at 300°C. Only the smaller reported mosaic angle is close to the mosaic angles obtained here by XRD. Discrepancies may be explained, on the one hand, since only one mosaic angle could be obtained by XRD due to the small separation of the Bragg peaks. Therefore, one of the oxide species may still exhibit a significant bigger mosaic angle which matches those obtained by SPA-LEED. On the other hand, SPA-LEED is a surface sensitive method. It is reasonable, that surface mosaics are stronger tilted than the bulk mosaics due to the lack of next neighbors. Since the topmost layers examined by SPA-LEED are contaminated with hydroxides during exposure to air these parts of the oxide films are destroyed and cannot

be investigated by ex situ XRD.

After annealing at 200°C and 300°C additional crystalline layers are formed within the films as confirmed by XRD and GIXRD. The Bragg peaks due to these crystalline layers are pointing to a tetragonally distorted cubic structure (in plane measurements not shown here) with lattice parameters of $a_{\perp} = 0.407\,nm$ and $a_{||} = 0.372\,nm$. Since no bulk praseodymia phase corresponds to these lattice constants, the formation of the additional crystalline layers have to be attributed to other influences except the reduction of the praseodymia film. We assume, that this layer is formed by contamination during air exposure since recent *in situ* investigations of the annealing process under high vacuum conditions (base pressure $1 \cdot 10^{-6}$ mbar, not shown here) do not exhibit any additional crystalline layer formation with the observed lattice parameters during annealing above 300°C.

It is well known that praseodymia powder is contaminated with hydroxides and hydroxy carbonates during air expose [25, 26]. These materials also show crystalline structures. Therefore, it is reasonable that the additional crystalline structures are formed at the top of the films as supported by XRR results. The mean density of $\delta = 8.7 \pm 0.2\,g/cm^3$ derived from XRR is also in the region of known Pr-hydroxides ($\delta = 8.75\,g/cm^3$ for Pr(OH)3)[25]. However, the lattice parameters disagree with known Pr-hydroxide as well as Pr-hydroxy carbonate bulk parameters, so that the observed crystalline structures cannot be attributed to particular materials. The occurrence of these structures only after annealing at 200°C and 300°C can probably be explained by the enhanced formation of stochastically distributed oxygen vacancies at higher annealing temperatures. Therefore, $PrO_{1.833}$ seems to be more stable against contamination than $PrO_{1.5}$ because it exhibit considerable less oxygen vacancies. It could, however, also be possible that increased surface roughness of these sample supports the formation of Pr-hydroxides or Pr-hydroxy carbonates.

Regarding the results of this work, two effects have to be taken into account concerning the decreased thickness of the crystalline oxide film: The contamination of the topmost mono layers of the film and the growth of the silicate interface layer with higher annealing temperatures. Both layers, however, increase more (about 2.7 nm) the oxide film thickness decreases (1 nm). For the Pr-silicate interface this can be explained by incorporation of SiO_2 compounds. Thus less praseodymium is necessary to form a new silicate layer since the Pr:O stoichiometry of this layer is smaller than for the crystalline oxide film. This is not the case if a crystalline oxide hydride layer is formed. Therefore, we assume that on top of the untreated

sample up to two mono layers are already contaminated with hydroxides, which could not be detected by XRD since they have *amorphous* structure. Furthermore, XRR alone may not be sufficiently sensitive to detect these layers due to the small layer thickness compared to the uncertainty of this method ($\pm 0.5\,nm$). Thus, the silicate layer formation seems to be overestimated in previous reports since the influence of contaminated praseodymia layers on top of the film was not taken into account. Here, additional investigations have to be performed to determine the crystalline structure and stoichiometry of the surface near layers and the exact influence on the loss of crystalline praseodymia material.

V. SUMMARY

In summary, we verified and extended the two-column model, which was previously developed to describe the phase separation of praseodymia films annealed in UHV [14]. The previous study used simple Bragg peak analysis with Gaussian functions, while we applied sophisticated analysis using the kinematic diffraction theory. Praseodymia films annealed up to 150°C are relaxed with a stoichiometry of $PrO_{1.833}$ and increased crystallite sizes. Further annealing finally results in a mixed crystalline film with both $PrO_{1.5}$ and $PrO_{1.5+\Delta}$ oxide species and decreased crystallite sizes since increasing lateral strain effects prohibit the release of oxygen from the compressed oxide phase. Full reduction to $PrO_{1.5}$ can only be obtained by further relaxation processes where strongly tilted mosaics are formed.

The amorphous Pr-silicate interface layer increases with higher annealing temperatures. This effect, however, seems to be smaller than reported before, since additional layers are formed close to the surface after annealing at 200°C and 300°C and subsequent exposure to ambient conditions. This effect is attributed to the contamination of the surface of the praseodymia films with hydroxides during exposure to air which leads to the formation of a hydroxide with cubic structure on top of the amorphous film. Further investigations are necessary to verify the origin and structure of this additional layer and to determine the influence on the crystalline film. Here, in situ annealing of the samples accompanied with XRD and XRR measurements seem to be an adequate method to perform studies under controlled ambient conditions.

VI. ACKNOWLEDGEMENT

XRR and XRD experiments were carried out at the synchrotron light source facilities DORIS III at HASYLAB/DESY. DESY is a member of the Helmholtz Association (HGF). We like to thank Wolfgang Calibe for assistance in using beamline W1 and Wolfgang Drube for assistance in using beamline BW2. We also acknowledge the Deutsche Forschungsgemeinschaft (DFG) for financial support via Graduate College 695 and Grant No. WO533/16.

Appendix A: Structure model and fitting parameter

Fig. 12 shows the structure model used to calculate the intensity of the specular diffraction rods $(00L)$ close to $L=2$. The main structure parameters, which are necessary to describe a single oxide species are the vertical lattice distance $d^{(i)}$ and the number of crystalline layers $N^{(i)}$ (cf. Fig.12). Here, the vertical lattice distance is derived by expanding (or compressing) the particular praseodymia bulk structure in (111)-direction (tetragonal distortion of unit cells). The entire diffraction signal from such a species is now obtained by *coherent* superposition of the waves scattered from all periodically arranged atoms. This leads to broad Bragg peaks and additional fringes due to the finite layer thickness. Furthermore, roughnesses at the bottom and at the top interface of each species are taken into account assuming a Gaussian distribution of the interface position. They are denoted as $\Phi_b^{(i)}$ and $\Phi_t^{(i)}$, respectively. The main effect of the interface roughness is an increased attenuation of the intensity of the fringes with increased deviation ΔL from the Bragg condition.

The film structure, used for the calculations in the presented work, at least consists of three different oxide species which are arranged in a particular way. First, the oxide film is split into two columns exhibiting different vertical layer constants $d^{(1)}$ and $d^{(2)}$. This is based on the fact that bulk praseodymia tends to form two coexisting oxide species with different stoichiometry and phase separation during phase transformation [23]. Whereas one of these columns (labeled column 2) is homogeneous the other (first) column is additionally split into a small oxide species (minority part) and a large oxide species (majority part) with different vertical lattice constants pointing to incomplete oxidized or reduced species. These species are stacked vertically and the diffracted signal is coherently superposed assuming that the vertical position of the interface between both species as well as the interface spacing are

well-defined. This can be assumed since pronounced fringes are observed close to the Bragg peaks pointing to homogeneous film thicknesses of the majority parts. Pronounced fringes can also be observed in XRR measurements which point to a homogeneous overall film thickness. A variation of the vertical interface position, which has to be modeled with many more than two columns, would lead either to a distribution of both the layer thickness of the minority and the majority part or to a distribution of the overall film thickness. In these cases, the fringes in XRD or XRR measurements should be drastically damped. Thus, distribution of several oxide species with considerably different vertical lattice constants and layer thicknesses is not considered since one expects no pronounced fringes close to the Bragg peaks.

The intensities diffracted from the homogeneous column and the inhomogeneous column are added up *incoherently* because a coherently summation approximately provides the same results since the mixed amplitude terms would vanish due to the large number of phase relations between the columns in reciprocal space (random phase approximation). The suggested phase separation is clearly visible for the untreated sample where two distinguished Bragg peaks can be observed (cf. Fig.4). The diffraction patterns from the other samples apparently exhibit only one obvious peak. Assuming only one oxide species to calculate the intensity distributions, however, the result does not match the measured intensity well. Here, the two column model clearly improves the agreement between calculated and measured intensity.

The obtained values for the structure parameters are presented in Tab. I. Homogeneous overall oxide film thicknesses can be calculated for each sample from the corresponding thicknesses of the single oxide species, which is in agreement with XRR measurements. The resulting layer distances increase with higher annealing temperature as expected for praseodymia unit cells with decreased oxygen content. Regarding the roughness of the majority oxide species, reasonable values can be derived from the intensity calculations, but they do not show a particular dependency on the annealing process. This effect may be attributed to the fact that the resulting roughnesses are not necessarily comparable since separate samples with slightly different initial interface roughnesses are used for each annealing step. Furthermore, it can be observed that the interface roughnesses obtained for the minority parts are large compared to their film thicknesses. Obviously, here the model with Gaussian distribution of the interface roughness is not that well suited to describe the

interface roughness is the layer thickness is small. Nevertheless, the results are reasonable.

Since the Si Bragg peak is kinematically forbidden at $L = 2$ only small intensity can be observed here. Therefore, structural parameters of the interface or the silicon substrate cannot be determined.

---

[1] J. Kwo, M. Hong, B. Busch, D.A. Muller, Y.J. Chabal, A.R. Kortan, J.P. Mannaerts, B. Yang, P. Ye, H. Gossmann, A.M. Sergent, K.K. Ng, J. Bude, W.H. Schulte, E. Garfunkel, and T. Gustafsson, J. Cryst. Growth **251**, 645 (2003).

[2] J. R. Stetter, W. R. Penrose, and S. Yao, J. Electrochem. Soc. **150**, 11 (2003).

[3] R. D. Kohn, Z. Pan, J. Sun, and C. Liang, Catalysis Communications **4**, 33 (2003).

[4] D.K. Fork, D.B. Fenner, and T.H. Geballe, J. Appl. Phys. **68**, 4316 (1990).

[5] A. Giussani, P. Rodenbach, P. Zaumseil, J. Dabrowski, R. Kurps, G. Weidner, H.-J. Muessig, P. Storck, J. Wollschlaeger, and T. Schroeder, J. Appl. Phys. **105**, 033512 (2009).

[6] T. Schroeder, T.-L. Lee, L. Libralesso, I. Joumard, and J. Zegenhagen, J Appl. Phys. **97**, 074906 (2005).

[7] T. Weisemoeller, C. Deiter, F. Bertram, S. Gevers, A. Giussani, P. Zaumseil, T. Schroeder, and J. Wollschläger, Appl. Phys. Lett. **93**, 032905 (2008).

[8] G.V. Antoshin, K.M. Minachev, and D.R. Dmitriev, Russ. Chem. Bull., **16**, 1793 (1967).

[9] K. Otsuka and M. Kunitomi, J. Catal. **105**, 525 (1987).

[10] Y. Takasu, M. Matsui, H. Tamura, S. Kawamura, Y. Matsuda, and I. Toyoshima, J. Catal. **69**, 51 (1981).

[11] Y. Takasu, M. Matsui, and Y. Matsuda, J. Catal. **76**, 61 (1982).

[12] Y. Borchert, P. Sonström, M. Wilhelm, H. Borchert, and M. Bäumer, J. Phys. Chem. C **112**, 3054 (2008).

[13] A.G. Dedov, A. S. Loktev, I. I. Moiseev, A. Aboukais, J.-F. Lamonier, and I. N. Filimonov, Appl. Cat. A: Gen. **245**, 209 (2003).

[14] S. Gevers, T. Weisemoeller, B. Zimmermann, F. Bertram, C. Deiter, and J. Wollschläger, J. Phys.: Condensed Matter **21**, 175408 (2009)

[15] L. G. Parratt, Phys. Rev. **95**, 359 (1954).

[16] H. Ono and T. Katsumata, Appl. Phys. Lett. **78**, 1832 (2001).

[17] T. Weisemoeller, F. Bertram, S. Gevers, C. Deiter, A. Greuling, and J. Wollschläger, Phys. Rev. B **79**, 245422 (2009).

[18] P. Zaumseil, J. Phys. D **41**, 135308 (2008).

[19] B. G. Hyde, E. E. Garver, U. E. Kuntz, and L. Eyring, J. Phys. Chem. **69**, 1667 (1965).

[20] D. A. Burnham and L. Eyring, J. Phys. Chem. **72**, 4415 (1968).

[21] R. G. Haire and L. Eyring, in: Handbook on the Physics and Chemistry of Rare Earths Vol. 18, K. A. Gschneidner, L. Eyring, G. R. Choppin and G. H. Lander(eds.), Elsevier Science B.V., 1994, Amsterdam, p.413.

[22] B. G. Hyde, D. J. M. Bevan, and L. Eyring, Philosophical Transactions of the Royal Society of London. Series A, Mathematical and Physical Sciences, **259**, 583 (1966).

[23] V. S. Rudenko and A. G. Boganov Inorg. Mater. (USSR) (Engl. Transl.), **7**, 98 (1971).

[24] R. P. Turcotte, J. M. Warmkessel, R. J. D. Tilley, and L. Eyring, J. Solid State Chem. **3**, 265 (1971).

[25] J.M. Haschke and L. Eyring, Inorg. Chem. **10**, 2267, (1971).

[26] Z.C. Kang and L. Eyring. J. Solid State Chem. **75**, 60, (1988). 90303-9.

[27] E. Summerville, R. Tuenge, and L. Eyring, J. Solid State Chem. **24**, 21 (1978).

[28] J. Zhang, R. B. Von Dreele, and L. Eyring, J. Solid State Chem. **122**, 53 (1996).

PDA temp.	species	N	$d^{(i)}$ [Å]	Φ_t [layers]	Φ_b [layers]
untreated	(1)	28.0	3.082	3.000	2.281
	(1')	3	3.148	2.229	0.470
	(2)	30	3.145	1.001	3.236
100°C	(1)	31	3.148	0.273	2.095
	(2)	31	3.161	1.786	1.927
150°C	(1')	2	3.186	0.517	1.963
	(1)	29	3.170	1.194	1.972
	(2)	30	3.164	1.958	1.405
200°C	(1)	24	3.233	2.008	3.697
	(1')	4	3.186	3.692	3.852
	(2)	28	3.183	0.727	3.769
300°C	(1)	24	3.277	0.487	3.205
	(1')	2	3.230	3.205	3.091
	(2)	27	3.239	1.738	1.284

TABLE I. Values obtained from the intensity distribution calculations of the untreated oxide films and the films annealed in UHV. The species denoted with single quotation marks are the minority oxide species of the corresponding column.

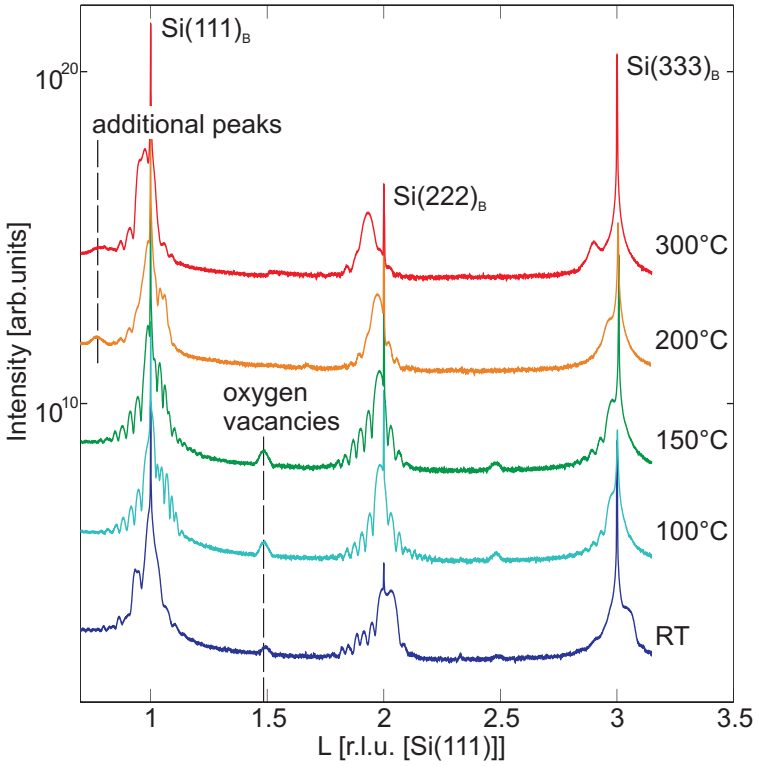

FIG. 1. XRD measurements in (00L)-direction of several samples annealed in UHV at temperatures ranging from RT to 300 °C. The Si Bragg peaks are labeled with bulk coordinates. The axis of abscissae is given in reciprocal lattice units of Si.

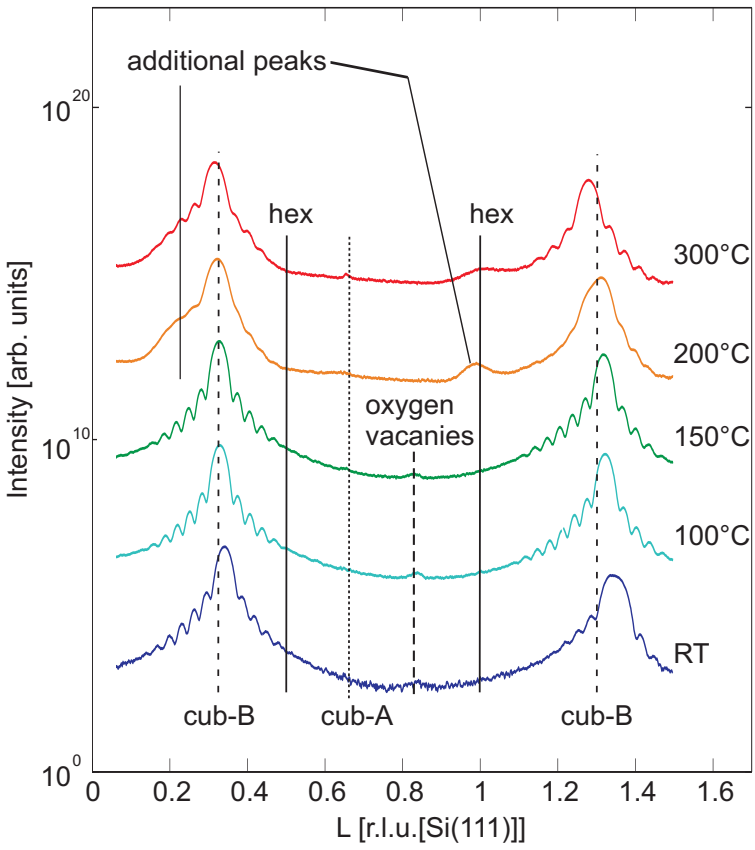

FIG. 2. GIXRD measurements of the CTRs in (01L)-direction from several samples annealed in UHV at temperatures from RT to 300 °C. Bragg peak positions are indicated for cubic Pr_2O_3 structure with A-type and B-type stacking (bottom) and for the hexagonal Pr_2O_3 structure (top). The axis of abscissae is given in reciprocal lattice units of Si.

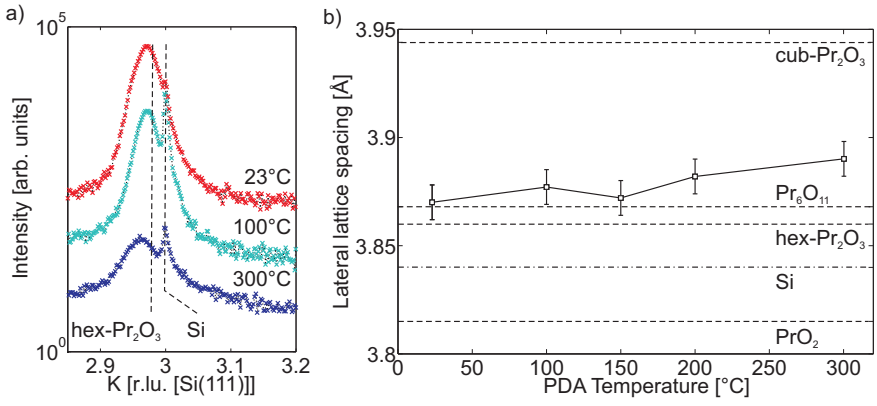

FIG. 3. (a) Exemplary experimental data from the untreated sample and the samples annealed at 100 °C and 300 °C. (b) Lateral lattice spacing of the oxide species derived from GIXRD in plane scans. Dashed lines indicate the bulk values of serveral oxide species.

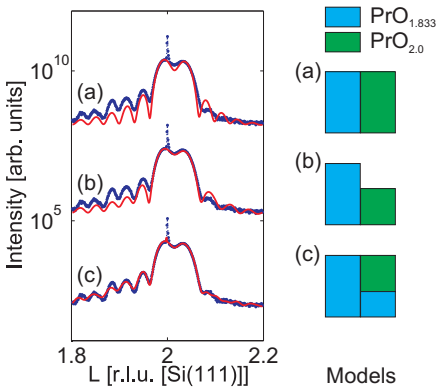

FIG. 4. Specular XRD (00L) measurements of the untreated sample at $L \approx 2$ and calculated fitting curves (solid lines) using different structure models.

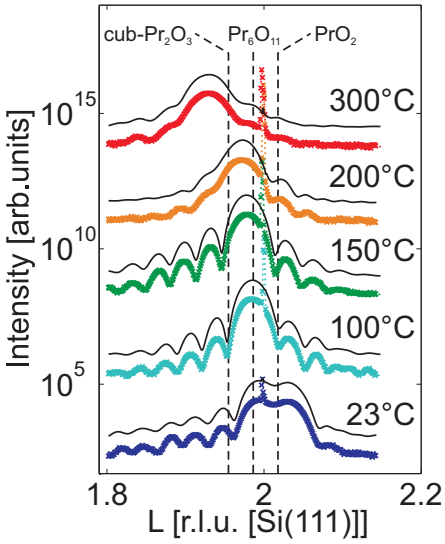

FIG. 5. Detailed view of the specular diffraction intensities at the region $L \approx 2$. The expected L positions for several praseodymia bulk phases are indicated.

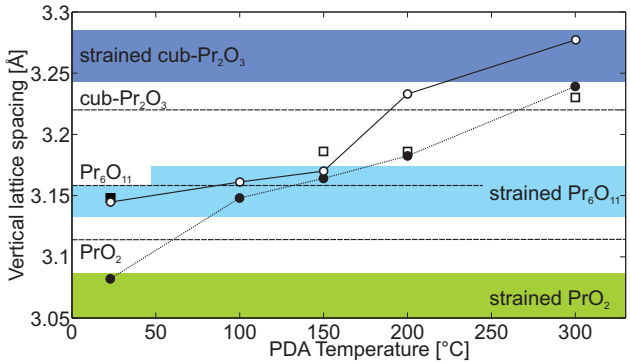

FIG. 6. Vertical lattice spacing of the oxide species during annealing in UHV. Dashed lines show the bulk values of several praseodymia species. The indicated areas present the corresponding lattice constants which are expected if strain effects are taken into account using the spread of lateral lattice constants obtained from in-plane scans. The value for the majority oxide parts are labeled with dots, whereas the minority crystalline parts are indicated with squares. Furthermore, full and open symbols indicate the crystalline parts of the first and second column, respectively.

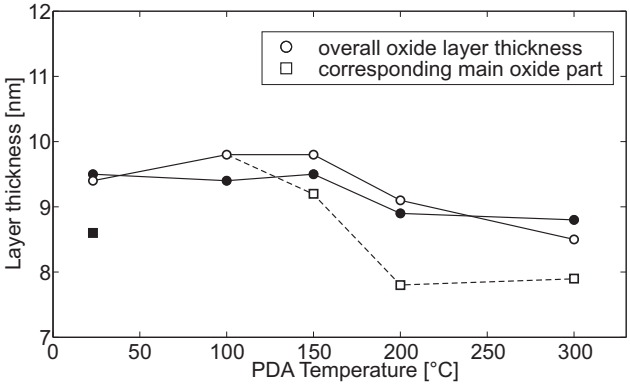

FIG. 7. Film thicknesses of both crystalline oxide parts. While solid lines show the overall oxide film thickness ($D_majority + D_minority$), the dashed lines indicate the corresponding majority oxide part $D_majority$. Full and open symbols indicate the crystalline parts belonging together.

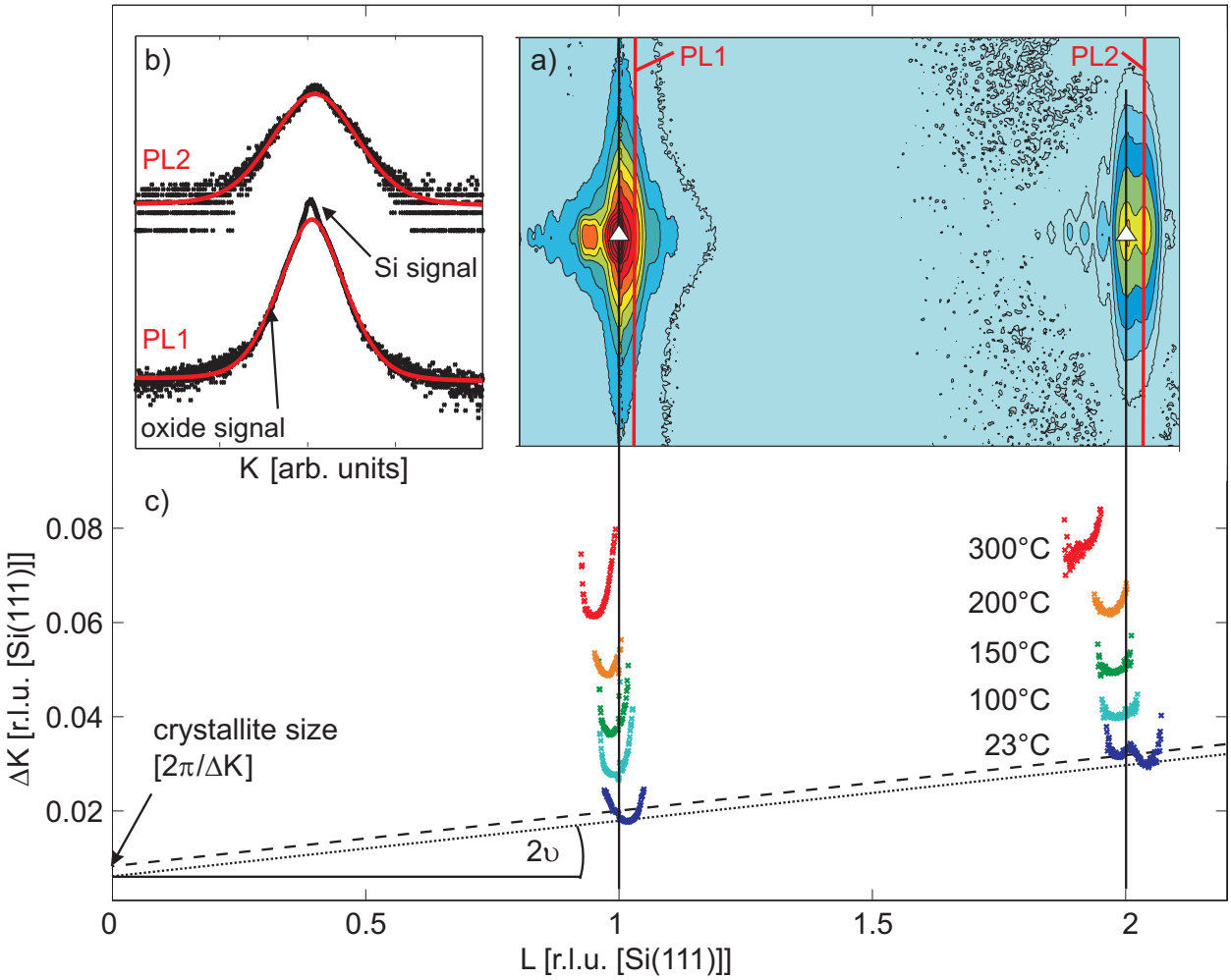

FIG. 8. (a) Reciprocal space map of the untreated sample in (00L) direction recorded by an 1-dimensional X-ray detector (Si Bragg peaks are labeled with triangles). (b) Exemplary line scans in parallel direction (black dots) and fitting curves (red lines) of the reciprocal space map at $L \approx 1$ and $L \approx 2$ (positions given in (c)). (c) FWHM of the diffracted intensity in $[00L]$ direction near the Bragg peak positions for several samples annealed at temperatures from RT to 300 °C. To illustrate the calculation process, dashed lines connect the minima of the FWHM at $L \approx 1$ and $L \approx 2$ for the untreated sample. Here, the mosaic angle and crystalline size of the oxide species can be derived via the gradient of the FWHM and the intersection of the dashed lines with the ordinate.

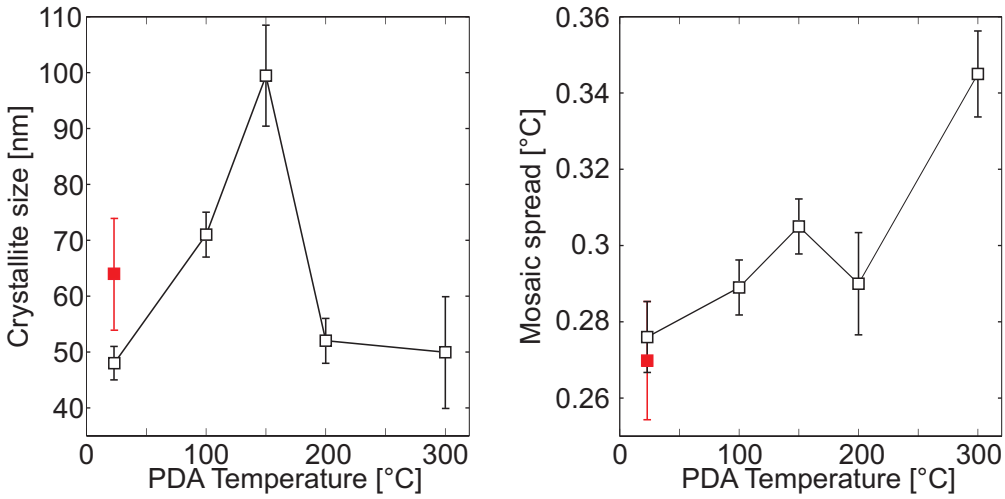

FIG. 9. Crystalline sizes and mosaic spread calculated from the L-dependence of the FWHM of the $(00L)$ rod.

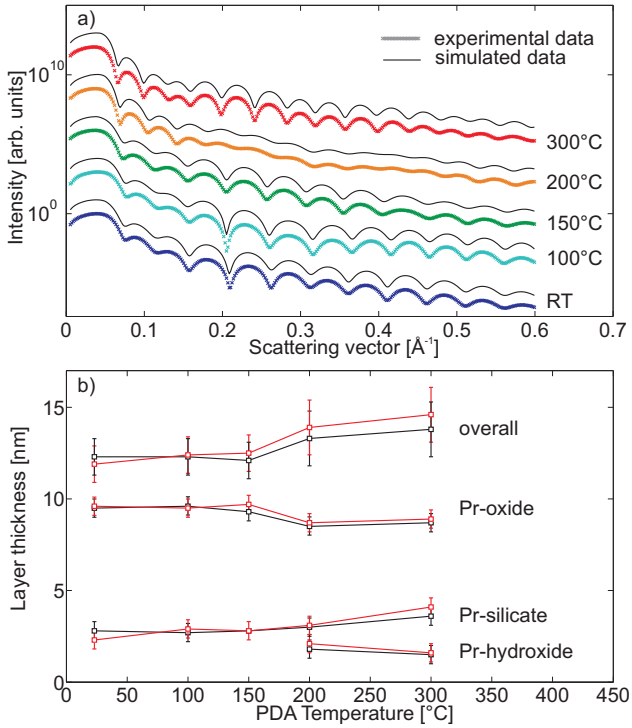

FIG. 10. (a) XRR measurements (crosses) and simulated fitting curves (solid lines) at several annealing temperatures in the range from RT to 300 °C. (b) Calculated film thicknesses of the film system components as determined with XRR.

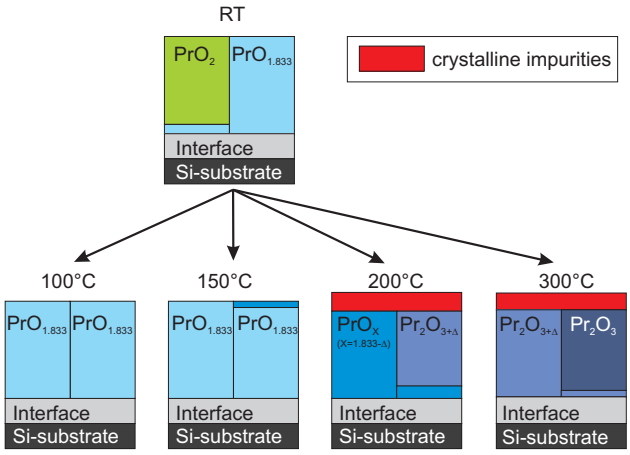

FIG. 11. Schematic illustration of the annealing processes. Please note, that each sample was annealed in one step from RT to the temperature under investigation.

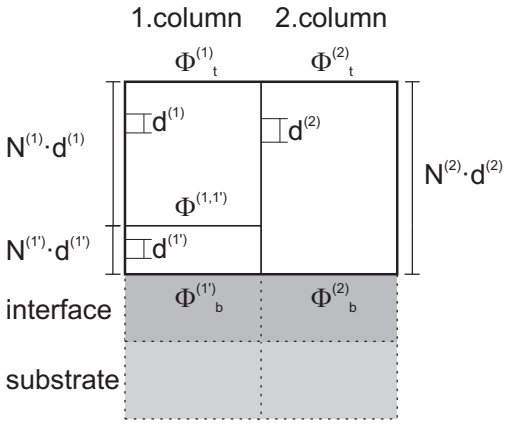

FIG. 12. Structure model used for the intensity calculations of the specular diffraction rods close to $L = 2$. The film is split into two laterally coexisting oxide species (1. column and 2. column). The first column is additionally split into two stacked oxide species with a majority part (1) and a minority part (1'). Each oxide species exhibits four main structure parameters used for the calculations of the intensity distributions. These are the layer distance $d^{(1)}$, the number of layers $N^{(1)}$ as well as the interface roughnesses $\Phi_t^{(1)}$ and $\Phi_b^{(1)}$ at the top and at the bottom of the species, respectively.